Article

Automated Analysis of Choroidal Sublayer Morphologic Features in Myopic Children Using EDI-OCT by Deep Learning

Junmeng Li[1,2], Lei Zhu[2,3], Ruilin Zhu[1], Yanye Lu[2], Xin Rong[1], Yadi Zhang[1], Xiaopeng Gu[1], Yuwei Wang[1], Zhiyue Zhang[1], Qiushi Ren[3], Bei Rong[1], and Liu Yang[1]

[1] Department of Ophthalmology, Peking University First Hospital, Beijing, China
[2] Institute of Medical Technology, Peking University Health Science Center, Peking University, Beijing, China
[3] Department of Biomedical Engineering, Peking University, Beijing, China

Correspondence: Liu Yang, Department of Ophthalmology, Peking University First Hospital, No. 8 Xi Shi Ku Street, Xicheng District, Beijing 100034, China.
e-mail: liu_yang@bjmu.edu.cn
Bei Rong, Department of Ophthalmology, Peking University First Hospital, No. 8 Xi Shi Ku Street, Xicheng District, Beijing 100034, China. e-mail: rongpei517@126.com

Purpose: The purpose of this study was to analyze the choroidal sublayer morphologic features in emmetropic and myopic children using an automatic segmentation model, and to explore the relationship between choroidal sublayers and spherical equivalent refraction (SER).

Methods: We collected data on 92 healthy children (92 eyes) from the Ophthalmology Department of Peking University First Hospital. The data were allocated to three groups: emmetropia ($+0.50$ diopters [D] to -0.50 D), low myopia (-0.75 D to -3.00 D), and moderate myopia (-3.25 D to -5.75 D). We performed standardized optical coherence tomography (OCT) and developed a new segmentation technique to measure choroidal thickness (CT), large-vessel choroidal layer (LVCL), medium-vessel choroidal layer (MVCL), and small-vessel choroidal layer thickness (SVCL), and evaluated the choroidal vascular system (choroidal vascular volume [VV], choroidal vascular index [CVI], and choroidal vascular density [CVD]).

Results: All choroidal sublayers (LVCL, MVCL, and SVCL) were significantly thinner in myopic than in emmetropic eyes ($P < 0.05$), the thinnest choroidal region being the nasal outer subfield ($P < 0.05$). In all choroidal regions of SVCL, a positive correlation was found between SER and thickness ratio ($P < 0.001$). In most subfields of MVCL, a similar correlation was found ($P < 0.050$), the exceptions being the two nasal subfields ($0.050 < P < 0.300$). In contrast, the thickness ratio of LVCL decreased in all subfields ($P < 0.050$). VV correlated with SER negatively in LVCL in all subfields (all $P < 0.001$) and most subfields in MVCL except for two temporal subfields ($0.050 < P < 0.200$). However, no significant correlations were found between CVI and SER in LVCL ($P > 0.050$) and MVCL (with the exception being the temporal inner subfield, $P = 0.011$).

Conclusions: Thickness of choroidal sublayers was reduced with higher myopic SER, whereas changes in thickness ratio varied between sublayers. No significant correlations between CVI and SER suggested that both choroidal stromal and vascular volume decreases proportionately.

Translational Relevance: Automatic segmentation model will be helpful for future clinical trials to quantify choroidal sublayer morphologic features in myopia.

Introduction

Myopia is a common public health problem globally, and especially in Asian countries.[1] Blindness and visual impairment caused by high myopia bring significant economic burden to all levels of society.[2] There is an urgent need to understand the mechanisms of myopia development and progression. Previous studies have shown that the choroid may play an

important role in regulating eye growth[3,4] and that changes in choroidal vascular sublayers may be related to the progression of myopia.[5,6]

Histologically, the choroid consists of three vascular sublayers: the innermost choriocapillaris, the medium-vessel (Sattler's) layer, and the large-vessel (Haller's) layer, which is connected to the choroidoscleral interface (CSI).[4] Optical coherence tomography (OCT) allows cross-sectional images of ocular tissues with micron resolution to be obtained in a noninvasive and noncontact manner. Furthermore, enhanced depth imaging OCT (EDI-OCT) promotes clear visualization of the choroid. Becauase the first use of EDI-OCT to visualize and quantitatively evaluate choroidal thickness (CT),[7] the technique has been used increasingly for this purpose and to evaluate the relationship between choroidal structures and ocular diseases.[4,6]

EDI-OCT enables the quantification of choroidal parameters, such as CT, choroidal volume (CV), choroidal vascular index (CVI), and choroidal vascular density (CVD). However, due to limitations in sublayer segmentation, research to date mainly focuses on the overall choroidal structures, rather than substructures. Studies using manual segmentation have shown that research on choroidal substructures helps to enhance understanding of eye disease mechanisms.[8–10]

For this reason, automatic segmentation of choroidal sublayers is of interest in the clinic. Manual segmentation has been used to observe Haller's and Sattler's layers on OCT B-scans[8] but this approach is limited by high variance and low repeatability. Subsequently, several studies utilized semi-automatic and automatic methods to achieve choroidal sublayers analysis,[11,12] including a method to detect the boundary between Haller's and Sattler's layers using exponentiation-based binarization.[11] Supplementary Table S1 summarizes the available literature on choroidal sublayers analysis in healthy subjects.

In summary, existing choroidal sublayers segmentation mainly relies on manual labels or binary-segmentation methods. The former strategy requires significant intervention by experienced doctors and cannot be used in large-scale samples. The latter can realize automatic segmentation but cannot analyze choroidal vascular characteristics and will be affected by the signal-to-noise ratio of OCT images. Therefore, we have developed a novel segmentation model based on deep learning and combining the benefits of manual and automated segmentation, which greatly improve performance for choroidal sublayers analysis in healthy children.

Materials and Methods

Participants

Clinical and imaging data were retrospectively collected from records of 92 healthy children (92 eyes) at the Ophthalmology Department of Peking University First Hospital. The study was approved by the Ethics Committee and complied with the Declaration of Helsinki.

All patients had undergone comprehensive ophthalmic examination, including anterior segment slit-lamp examination and fundus ophthalmoscopy. Axial length was measured using the IOL Master (Carl Zeiss Meditec AG, Jena, Germany). Under cycloplegia, refractive error was measured using an auto-refractometer (RM8900; TOPCON). If both eyes met the inclusion and exclusion criteria, only the right eye was analyzed. The data were divided into three groups according to the spherical equivalent refraction (SER): emmetropia (+0.50 D to −0.50 D), low myopia (−0.75 D to −3.00 D), and moderate myopia (−3.25 D to −5.75 D).

The eligibility criteria for selection of patients' records were as follows: age 8 to 16 years old, with normal findings on fundus and OCT examination. The exclusion criteria were: ocular pathology, hypertension, diabetes or other systemic diseases, myopia above −6.0 D, and history of intraocular surgery or injection.

EDI-OCT Image Acquisition

The dataset was obtained using enhanced depth imaging mode of the Spectralis OCT (Heidelberg Engineering, Heidelberg, Germany). A total of 31 raster scans centered on the fovea were performed, covering a 20 × 20 degree visual field (6 × 6 mm). A single B-scan consisted of 768 A-scans (high-speed mode). To improve the signal-to-noise ratio, automatic real-time tracking was used with 30 frames averaged for each scan.

The OCT image set needed to be of sufficient quality to segment the choroid. If the right eye image was of insufficient quality, the left eye image would be selected.

Manual Choroidal Sublayers and Vessels Segmentation Protocol

The choroid was visualized on the EDI-OCT B-scan image and subdivided into large, medium, and small vessel choroidal layers (LVCL, MVCL, and SVCL, respectively) using a manual segmentation protocol
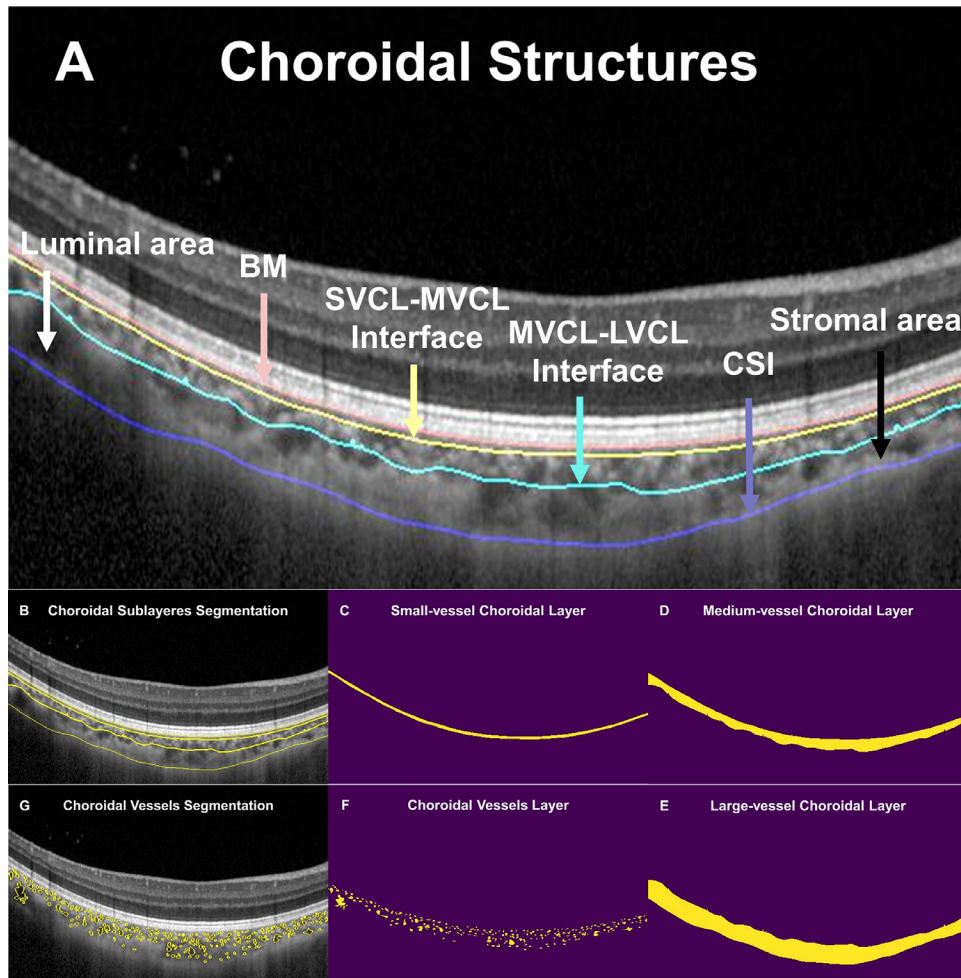
Figure 1. Illustration of manual segmentation of choroidal sublayers and vessels in OCT images. SVCL consists of indistinguishable choroidal small vessels on the inner side of MVCL and choriocapillaris just below the retinal pigment epithelium (RPE). Total choroid is defined as the distance between BM and CSI. The boundary between SVCL and the MVCL is parallel to BM. The LVCL is defined as the external choroid, which is composed of large and low signal space that represents the large vascular lumen. The MVCL consists of medium-sized hypo-intense space, surrounded by a hyper-intensive stroma with increased scattering of high-density melanocytes that show a mottled appearance. The mottled appearance signal in OCT B-scans helps to distinguish LVCL from MVCL. (**A**) Detailed illustrations of choroidal structures. (**B–E**) Choroidal sublayers boundary segmentation and visualization images. (**F, G**) Choroidal vessels segmentation and visualization images. BM, Bruch's membrane; CSI, choroidoscleral interface; SVCL-MVCL interface, interface of small-vessel choroidal layer and medium-vessel choroidal layer; MVCL-LVCL interface, interface of medium-vessel choroidal layer and large-vessel choroidal layer.

based on previous work.[8,13,14] Detailed protocols of manual segmentation are provided in the Supplementary Materials. Image-based cues used in this protocol to distinguish the layers and structures are detailed in Figure 1. Two experienced ophthalmologists (authors Z.Y. and G.X.) were trained in the protocol before manual segmentation of OCT choroidal images. For each subject, one B-scan was selected. In total, 92 images were selected for the manual annotation, consisting of 937,505 labeled pixel annotations in 11,746 choroidal vessels fragments. As for boundaries

segmentation, 273,846, 864,025, and 2,120,429 labeled pixel annotations were included in small-, medium-, and large-vessel layers, respectively.

Automatic Choroidal Sublayers and Vessels Segmentation Model

We apply the learning-based method to obtain choroidal vessels and stroma of different choroidal sublayers. Assuming that the input B-scan is $X_i \in \mathbb{R}^{H \times W}$, two deep convolutional neural networks
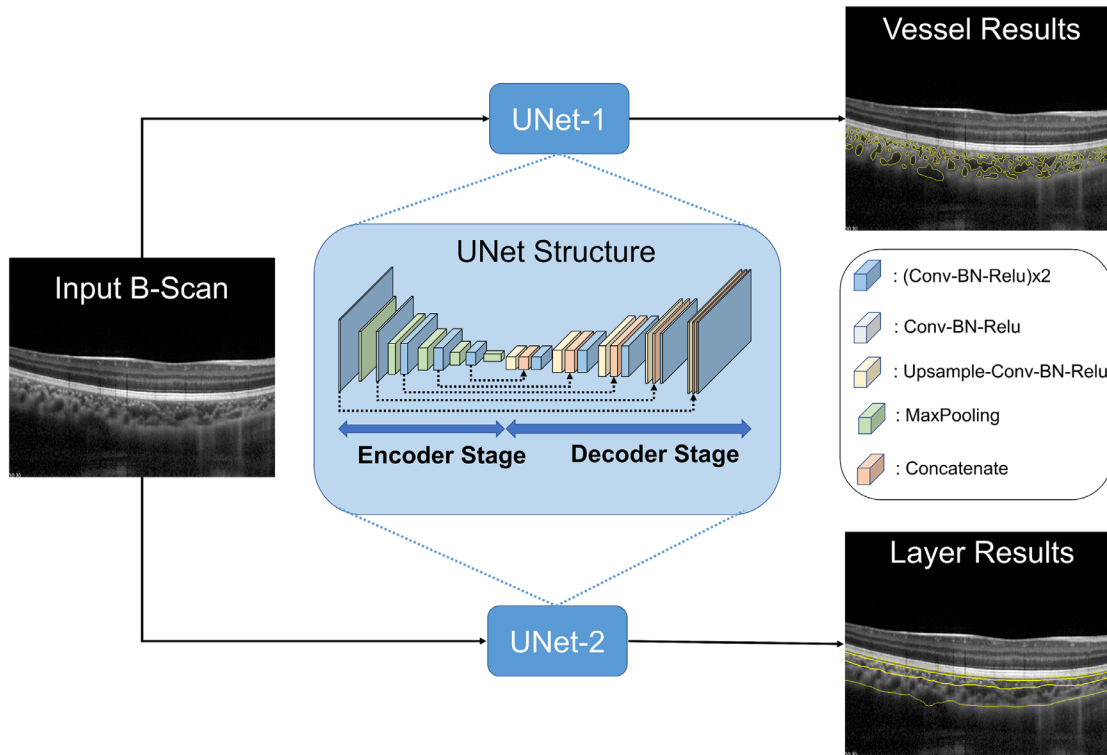
Figure 2. Principle of automatic choroidal sublayers and vessels segmentation model by deep learning. The encoder stage contains five encoder modules that implemented as two serials of convolutional operation (Conv), batch normalized (BN), and rectified linear unit (ReLU) activation. Meanwhile, the decoder stage decoder also contains five decoder modules which firstly up-sample the input feature and concatenate it with the output feature from the corresponding encoder stage. Then, Conv operator, BN, and ReLU are used to fuse the concatenate features and forms the output.

(DCNNs) are trained to obtain segmentation of sublayers P_i^1 and of the choroid P_i^2, respectively. In the training step, cross entropy loss is used to supervise the training step of the two DCNNs with the help of their corresponding human-labeled ground-truths Y_i^1 and Y_i^2, which may be formulated as:

$$Loss(P, Y) = -\sum_i Y_i \log(P_i) + (1 - Y_i) \log(1 - P_i).$$

Specifically, our network uses a UNet backbone structure containing an encoder stage to extract high-level features and a decoder stage to reconstruct the resolution. Detailed working principle is shown in Figure 2.

As for the hyperparameters, channel number 64, 128, 256, 512, and 1024 were set for the encoder stage and corresponding decoder stage. The up-sampling strategy was implemented as bilinear interpolation, and the SGD optimizer with a learning rate of 0.01 is used in the training of both two DCNNs. Sixty-four samples labeled by experts served as ground-truth for the training step and the other 28 samples served as the test sets to evaluate the effectiveness of our method

(note that for the analysis parts, all 92 samples are used for training for higher precision).

Choroidal Biomarkers

To investigate morphologic features of choroidal sublayers, we applied four biomarkers:

1) Choroidal thickness (CT): the distance between the upper and lower boundaries were used to compute the CT biomarker, which may be formulated as:

$$CT_{in} = \left[\arg\max_j Y_n^1(i, :) - \arg\min_j Y_n^1(i, :) \right] * L_j$$

where i, n, and j are the indices of crosswise, longitudinal and depth dimensions. Y_n^1 is the sublayer segmentation result for the B-scan.

Based on CT results, we can calculate the ratio of each choroidal sublayer thickness to the total CT, namely thickness ratio.

2) Choroidal volume (CV) and vascular volume (VV): the volume of the choroid and choroidal vessels for each sublayer was also calculated, and formulated as:

$$CV_{in} = \sum_j Y_n^1(i, j) * L_i * L_n * L_j$$

$$VV_{in} = \sum_j Y_n^2(i, j) * L_i * L_n * L_j$$

where i, n, and j are the indices of crosswise, longitudinal, depth. Y_n^1 is the sublayer segmentation result for the B-scan and Y_n^2 is the segmentation result of vessels. L_i, L_n, and L_j are crosswise, longitudinal, and depth dimensions.

3) CVI: the ratio of the choroidal vascular luminal volume to the total CV is used as the CVI biomarker, defined as:

$$CVI_{in} = \frac{\sum_j \left[Y_n^2(i, j) * Y_n^1(i, j) \right]}{\sum_j Y_n^1(i, j)}$$

where Y_n^2 is the segmentation result of vessels, and Y_n^1 is the choroidal sublayer segmentation result.

Especially, the three-dimensional CVI reflects the volumetric CVD.

4) CVD: The choroidal vessels map was projected into the crosswise-longitudinal space. We then normalized the projected results to the maximum value and used Otsu binary segmentation method to obtain the CVD.[15]

Our preliminary experimental results showed that the interscan distance of 240 microns was enough to perform quantitative assessments in the Early Treatment of Diabetic Retinopathy Study (ETDRS) subfields (Supplementary Table S2[1–5]). The mean CT, CV/VV, CVI, and CVD in choroidal sublayers were calculated in each of the 9 subfields of ETDRS grid covering the fundus area of 6 × 6 mm. These nine subfields are central (C), superior inner (SI), temporal inner (TI), inferior inner (II), nasal inner (NI), superior outer (SO), temporal outer (TO), inferior outer (IO), and nasal outer (NO).

Statistical Analysis

The efficiency of the proposed method was evaluated by comparing the automatic segmentation model with manual segmentation. Specifically, we use the accuracy (ACC), sensitivity (SE), specificity (SP), precision (PC), and dice coefficient (DC) between the algorithm segmentation and the manual reference as the metric.

In our study, SER is defined as sphere power plus half negative cylinder power. Frequencies and descriptive statistical methods were used to analyze the demographic and imaging data of healthy children. SPSS statistical software for windows, version 23.0 (IBM Corp., Armonk, NY, USA) was used to conduct normality tests, Pearson's or Spearman's correlation analyses, and 1-way ANOVA tests. Differences between categorical data were evaluated using the chi-squared tests. The possible contributions of independent variables (such as spherical equivalent refraction and axial length) to the choroidal biomarkers were analyzed using linear regression analysis. A value of $P < 0.05$ was considered statistically significant.

Results

Effectiveness of Automatic Segmentation Model by Deep Learning

Five examples of test sample segmentation results are shown in Supplementary Figure S1. The results indicate clear segmentation of the choroidal sublayers and vessels, distinction of blood vessel type, and preserved boundaries of the choroid vessels. Quantitative results show that the sublayers segmentation can obtain 0.987 ACC and 0.959 DC scores on all the test samples compared with manual segmentation ground truth. For the more complex segmentation of choroidal vessels, our method still achieves 0.980 ACC with 0.699 DC scores (Supplementary Table S3).

Summary of Demographic and Ocular Characteristics

No significant difference in age or gender distribution was found between the three groups. AL increased with SE, and significant differences were found between the three groups ($P < 0.01$; Table 1).

Choroidal Sublayer Biomarkers Analysis

Choroidal Thickness in the Three Groups

Tables 2A, 2B, and 2C shows thickness of choroidal sublayers at each of the nine regions. In both SVCL and MCVL, differences between emmetropia and low myopia were not significant in any subfield (all $P > 0.050$). Significant differences were found between emmetropia and moderate myopia, low myopia, and

Table 1. Demographic and Ocular Biological Parameters in Emmetropia, Low, and Moderate Myopia Groups

Characteristics	Emmetropia Group $N = 22$	Low Myopia Group $N = 36$	Moderate Myopia Group $N = 34$	P Value
Age (y)	10.42 ± 1.66	10.52 ± 1.56	11.09 ± 2.11	0.295
Gender (male) (%)	45.5	58.3	44.1	0.230
Ocular biological parameters				
SER (D)	−0.05 ± 0.37	−2.15 ± 0.52	−4.12 ± 0.76	**<0.01**
AL (mm)	23.54 ± 0.74	24.46 ± 0.82	25.24 ± 0.78	**<0.01**

The chi-squared test for gender, 1-way ANOVA test for age, SER, and AL.
Statistically significant P values are shown in bold.
D, diopter; SER, spherical equivalent refraction; AL, axial length.

Table 2A. Comparison of Small-Vessel Choroidal Layer Thickness Between Different Groups

	SVCL Thickness, μm			P Value		
	Group 1	Group 2	Group 3	Group 1 vs. Group 2	Group 1 vs. Group 3	Group 2 vs. Group 3
Central	22.85 ± 0.61	23.00 ± 0.76	22.03 ± 1.25	0.794	**0.005**	**0.001**
Superior Inner	22.75 ± 0.55	22.84 ± 0.68	21.89 ± 1.21	0.934	**0.002**	**0.001**
Temporal Inner	22.51 ± 0.89	22.20 ± 0.94	21.76 ± 1.16	0.773	**0.024**	0.218
Inferior Inner	22.82 ± 0.61	22.80 ± 0.67	21.90 ± 1.19	1.000	**0.001**	**0.001**
Nasal Inner	22.46 ± 1.32	22.57 ± 0.96	21.29 ± 1.59	0.982	**0.012**	**<0.001**
Superior Outer	22.42 ± 0.68	22.43 ± 0.74	21.55 ± 1.21	1.000	**0.003**	**0.002**
Temporal Outer	21.46 ± 1.28	21.69 ± 1.31	21.35 ± 1.74	1.000	1.000	1.000
Inferior Outer	22.54 ± 0.79	22.41 ± 0.67	21.63 ± 1.11	0.885	**0.002**	**0.003**
Nasal Outer	21.10 ± 1.55	20.79 ± 1.31	19.75 ± 1.55	1.000	**0.003**	**0.012**

Table 2B. Comparison of Medium-Vessel Choroidal Layer Thickness Between Different Groups

	MVCL Thickness, μm			P Value		
	Group 1	Group 2	Group 3	Group 1 vs. Group 2	Group 1 vs. Group 3	Group 2 vs. Group 3
Central	75.28 ± 11.19	74.92 ± 13.10	57.77 ± 10.64	1.000	**<0.001**	**<0.001**
Superior Inner	73.88 ± 9.62	73.69 ± 10.87	58.04 ± 10.55	1.000	**<0.001**	**<0.001**
Temporal Inner	74.08 ± 11.46	74.01 ± 10.27	62.61 ± 11.85	1.000	**0.001**	**<0.001**
Inferior Inner	73.85 ± 8.71	74.03 ± 11.39	57.88 ± 11.03	1.000	**<0.001**	**<0.001**
Nasal Inner	70.93 ± 10.36	69.10 ± 12.72	55.20 ± 12.80	1.000	**<0.001**	**<0.001**
Superior Outer	72.95 ± 8.88	71.79 ± 8.72	58.74 ± 9.06	1.000	**<0.001**	**<0.001**
Temporal Outer	76.64 ± 11.71	75.67 ± 9.24	65.41 ± 7.82	1.000	**<0.001**	**<0.001**
Inferior Outer	73.63 ± 8.36	71.72 ± 9.49	58.45 ± 9.60	1.000	**<0.001**	**<0.001**
Nasal Outer	62.29 ± 12.68	58.70 ± 10.75	50.74 ± 8.40	0.622	**<0.001**	**0.006**

moderate myopia in SVCL in almost all subfields ($P < 0.020$; the exception being TI or TO, $P > 0.050$) and in all subfields without exception in MVCL (all $P < 0.010$; Tables 2A, 2B).

In contrast, LVCL was significantly different between emmetropia and low myopia in most subfields (the exceptions being the TI and NO ($P = 0.137$ and $P = 0.667$, respectively, which were the same as total

CTs; Supplementary Table S4) and between emmetropia and moderate myopia, low myopia, and moderate myopia in all subfields (all $P < 0.010$; Table 2C).

Relationship Between Choroidal Thickness and Spherical Equivalent Refraction

A simple linear regression model was used to analyze the relationship between SER and CT

Table 2C. Comparison of Large-Vessel Choroidal Layer Thickness Between Different Groups

	LVCL Thickness, µm			P Value		
	Group 1	Group 2	Group 3	Group 1 vs. Group 2	Group 1 vs. Group 3	Group 2 vs. Group 3
Central	215.61 ± 42.97	185.97 ± 37.21	144.37 ± 30.23	**0.010**	**<0.001**	**<0.001**
Superior Inner	214.07 ± 39.73	186.17 ± 35.37	144.73 ± 29.81	**0.011**	**<0.001**	**<0.001**
Temporal Inner	215.86 ± 37.87	196.10 ± 36.22	156.23 ± 34.56	0.137	**<0.001**	**<0.001**
Inferior Inner	214.34 ± 41.26	185.60 ± 33.70	144.98 ± 29.74	**0.008**	**<0.001**	**<0.001**
Nasal Inner	189.11 ± 42.82	163.47 ± 27.39	134.03 ± 27.01	**0.011**	**<0.001**	**0.001**
Superior Outer	206.98 ± 37.01	180.88 ± 31.43	143.74 ± 28.49	**0.010**	**<0.001**	**<0.001**
Temporal Outer	223.19 ± 45.32	191.42 ± 34.85	160.03 ± 32.02	**0.006**	**<0.001**	**0.002**
Inferior Outer	205.80 ± 38.54	179.99 ± 27.85	144.42 ± 27.46	**0.007**	**<0.001**	**<0.001**
Nasal Outer	142.44 ± 38.63	132.28 ± 27.08	106.53 ± 28.13	0.667	**<0.001**	**0.002**

Group 1: emmetropia group; group 2: low myopia group; group 2: moderate myopia group.
All values are presented as the mean ± standard deviation.
Statistically significant changes between different groups by 1-way ANOVA with the Bonferroni post hoc test and Dunnett's T3 post hoc test.
Statistically significant P values are shown in bold.

(Fig. 3, Supplementary Table S5). SVCL thickness exhibited significant negative correlations with SER in all subfields ($0.301 \leq r \leq 0.421$, all $P < 0.020$), except for TO ($r = 0.192$, $P = 0.648$; see Fig. 3). SVCL thinning was most marked at the NO subfield at 0.345 µm per diopter ($P < 0.001$, 95% confidence interval [CI] = 0.165–0.526 µm) and least at the TI subfield at 0.159 µm per diopter ($P = 0.014$, 95% CI = 0.033–0.286 µm; Supplementary Table S5-1).

MVCL thickness was negatively correlated with SER in all nine subfields ($0.353 \leq r \leq 0.520$, all $P < 0.010$; see Fig. 3). Thinning was most marked in the center subfield at 4.042 µm per diopter ($P < 0.001$, 95% CI = 2.459–5.625 µm), and least in the TO subfield at 2.476 µm per diopter ($P < 0.001$, 95% CI = 1.250–3.702 µm; Supplementary Table S5-2).

Similarly, LVCL thickness reduced with SER in all nine subfields ($0.341 \leq r \leq 0.621$, all $P < 0.001$; see Fig. 3). Thinning was most marked in the center subfield at 16.876 µm per diopter ($P < 0.001$, 95% CI = 12.407–21.346 µm) and least in the NO subfield at 8.025 µm per diopter ($P < 0.001$, 95% CI = 4.165–11.885 µm; Supplementary Table S5-3).

Correlation of Choroidal Thickness Ratio With Spherical Equivalent Refraction

As illustrated in Figure 4, MVCL thickness ratio was positively correlated with SER in almost all subfields ($P < 0.050$; the exception being the central and NI and outer subfields ($P = 0.077$, $P = 0.615$, and $P = 0.295$, respectively) and in all subfields without exception in SVCL (all $P < 0.010$). On the contrary,

LVCL thickness ratio was negatively correlated with SER in all nine subfields (all $P < 0.050$).

Choroidal and Vascular Volumes

The difference of CV in different groups is similar to CT (Supplementary Table S6[1–3]). The characteristics of choroidal VV are shown in Supplementary Table S7. In MVCL, VV was similar in emmetropia and low myopia (all subfields $P > 0.050$). In contrast, significant differences in VV were found between emmetropia and moderate myopia in most subfields ($P < 0.050$) except for TI and TO ($P = 0.475$ and $P = 0.218$, respectively) and between low myopia and moderate myopia in most subfields (all $P < 0.010$) except for TI, NI, and NO ($P = 0.256$, $P = 0.075$, and $P = 0.055$, respectively; Supplementary Table S7-1).

VV differences between groups were identical within LVCL and for the total choroidal VV, with significant difference between emmetropia and low myopia in most subfields except for TI ($P = 0.131$) and between emmetropia and moderate myopia in all subfields ($P < 0.050$). Significant differences in VV were also found between low myopia and moderate myopia in most subfields ($P < 0.050$), except for TO, NI, and NO ($P = 0.080$, $P = 0.073$, and $P = 0.307$, respectively; Supplementary Table S7-2).

Choroidal Vascular Index

CVI was similar between groups in MVCL in all subfields (all $P > 0.050$) and in most subfields in LVCL, the exception being a significant difference in the NO
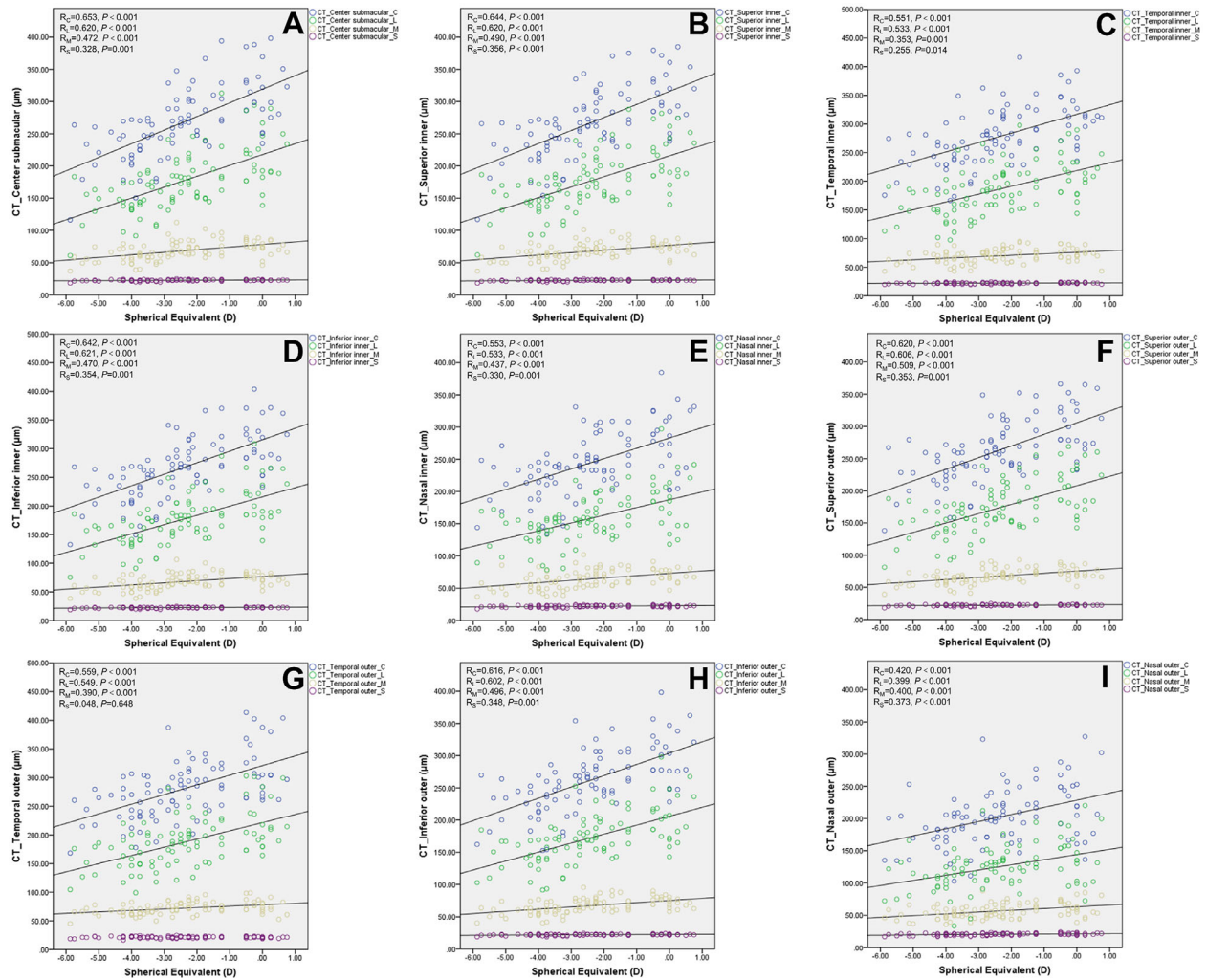
Figure 3. Scatter plots showing the mean choroidal thickness of choroidal sublayers in the nine ETDRS subfields as a function of spherical equivalent refraction. Panels **A** to **I** represent the Center, Superior Inner, Temporal Inner, Inferior Inner, Nasal Inner, Superior Outer, Temporal Outer, Inferior Outer, and Nasal Outer subfields, respectively. CT, choroidal thickness; μm, micron; D, diopter. *Blue dots* represent total choroidal thickness; *green dots* LVCL thickness; *orange dots* MVCL thickness; and *purple dots* SVCL thickness.

subfield between emmetropia and low myopia ($P < 0.001$; Supplementary Table S8[1–2]).

In MVCL, CVI was correlated negatively with SER in the TI subfield only ($P = 0.011$) and positively with AL in the TI and TO subfields ($P = 0.029$ and $P = 0.023$, respectively). No other significant correlations between CVI and SER or AL were found in LVCL and total choroid (Supplementary Table S9).

Choroidal Vascular Density

In MVCL, CVD was similar in emmetropia and low myopia in all subfields ($P > 0.050$) and between emmetropia and moderate myopia in most subfields, the exception being the center ($P = 0.035$). Significant differences were also found between low myopia and

moderate myopia in the center, II, and SI subfields only ($P = 0.006$, $P = 0.035$, and $P = 0.002$, respectively).

In contrast, in LVCL and total layers (MVCL and LVCL) significant differences were found between emmetropia and low myopia in the center, superior, II, and NO subfields (all $P < 0.050$), between emmetropia and moderate myopia in the superior and inferior subfields ($P < 0.050$), and between low myopia and moderate myopia in the NO subfield ($P = 0.038$; Supplementary Tables S10, S11).

Discussion

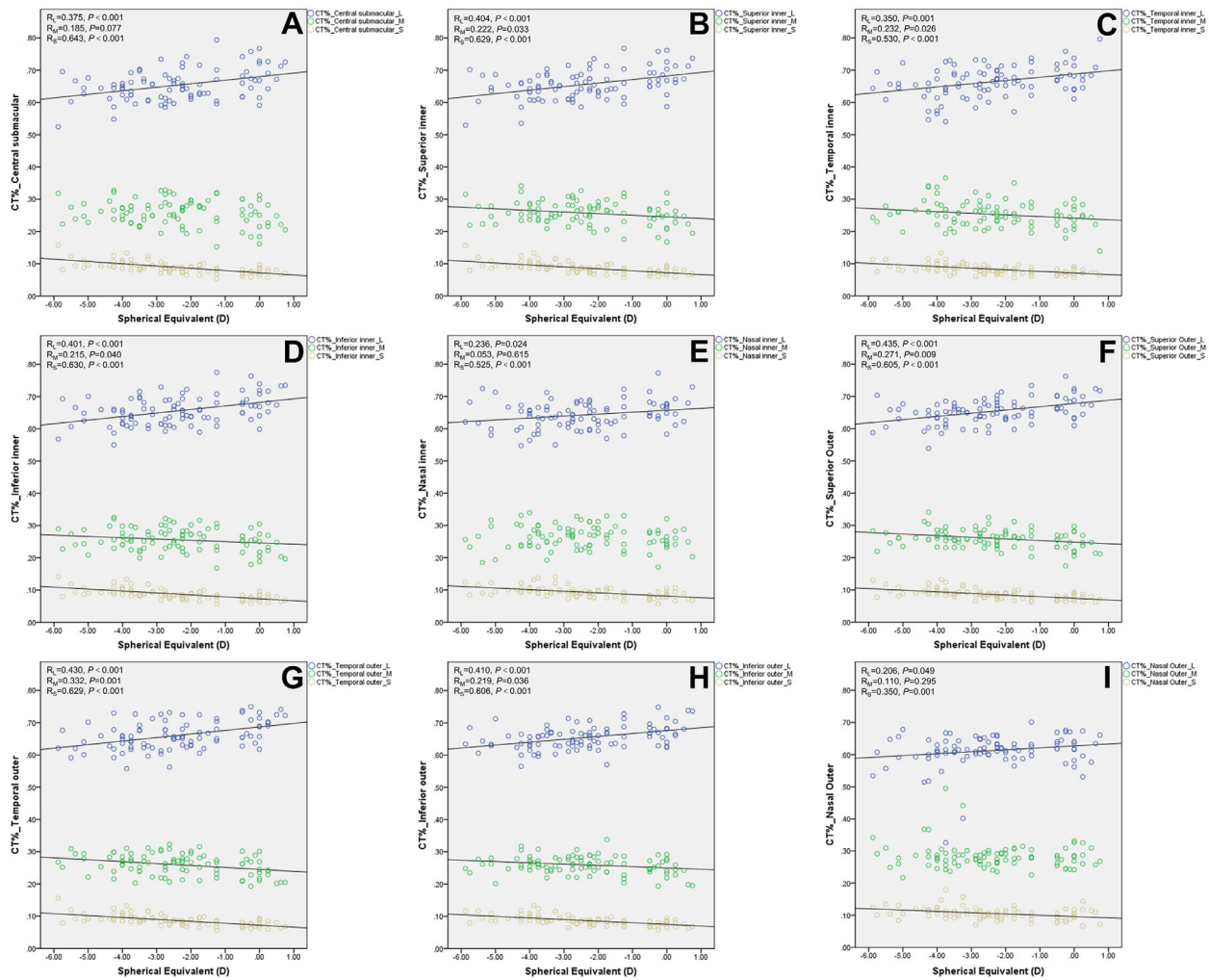In this study, a new automatic segmentation technique realizes automatic quantification of

Figure 4. Scatter plot showing thickness ratio of choroidal sublayers in the nine ETDRS grid subfields as a function of spherical equivalent refraction. Panels **A** to **I** represent the Center, Superior Inner, Temporal Inner, Inferior Inner, Nasal Inner, Superior Outer, Temporal Outer, Inferior Outer, and Nasal Outer subfields, respectively. CT%, choroidal thickness ratio; D, diopter. *Blue dots* represent LVCL thickness ratio; *green dots* MVCL thickness ratio; and *orange dots* SVCL thickness ratio.

choroidal sublayers and vascular characteristics based on deep learning. Our results are consistent with those obtained manually. The proposed method shows high accuracy (0.980 or over) and could greatly reduce the time consumption and material costs, requiring only 64 manually labeled B-scans for training. Therefore, our automatic segmentation method can support the analysis of choroidal structure in a large normal database of OCT images.

At present, CTs described by manual segmentation are mostly limited to the foveal and macular regions. Similar to C-scans in en face OCT, our method allows large scale face projection and three-dimensional volume rendering, with the potential to enhance understanding of the choroidal vascular system. In addition, the study about the variability of choroidal vascular layer thickness is more reasonable, avoiding choroidal

fragmentation information and local morphological details of the traditional longitudinal B-scans.[8,9,11,16] Our findings on CT were largely consistent with those of previous studies using manual or automatic methods.[8,11,17] However, CT was greatest in the TI or TO subfields in the present study, whereas LVCL thickness was greatest at the subfovea in a previous study using single B-scan images.[8] A possible explanation for this discrepant finding is that single B-scan measurements cannot well describe the variability of CT distribution.

In addition, Alshareef et al. found no significant difference in LVCL thickness between myopia and control groups,[6] contrary to our study in which significant differences were found between low and moderate myopia. Variations between subfields and differences in segmentation methods may partly explain these
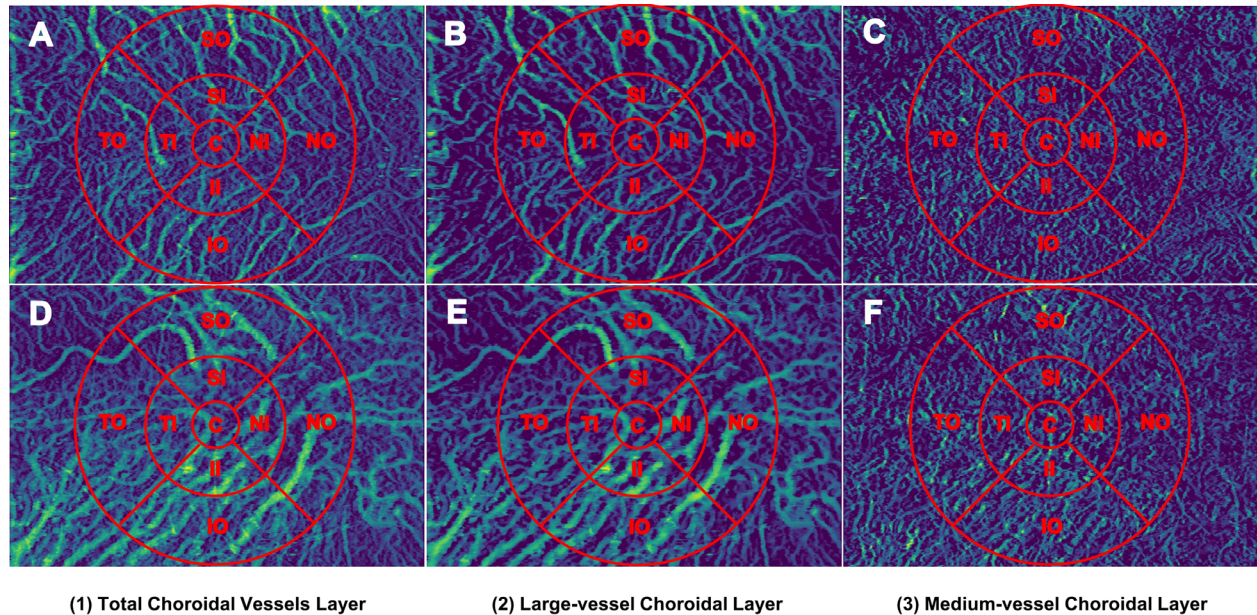
Figure 5. Two examples of choroidal vascular visualization images of the total choroidal vessels layer, large-vessel choroidal layer and medium-vessel choroidal layer. Children with emmetropia and moderate myopia were measured by EDI-OCT with 11.5 μm scan spacing. (**A–C**) Children with moderate myopia; (**D–F**) children with emmetropia; **A** and **D** total choroidal vessels layer (not including small-vessel choroidal layer); **B** and **E** large-vessel choroidal layer; **C** and **F** medium-vessel choroidal layer. The grid centers on the fovea, covering the fundus area of 4.5 × 4.5 mm. The diameter of the central, inner, and outer circle was 0.75 mm, 2.25 mm, and 4.5 mm, respectively. C (Central), **SI** (Superior Inner), **TI** (Temporal Inner), **II** (Inferior Inner), **NI** (Nasal Inner), **SO** (Superior Outer), **TO** (Temporal Outer), **IO** (Inferior Outer), and **NO** (Nasal Outer).

contrasting findings. Mean MVCL thickness measured in this study was much thicker than our results. Histological[18] and indocyanine green angiography (ICGA)[19] studies have also found a reduction and attenuation of choroidal large vessels in myopia, consistent with the present finding.

Our automated segmentation technique allows detailed investigates of the choroidal sublayers. Multiple studies have reported a negative correlation between CTs and refractive error[6,20,21] and the present study generally supports these findings. A possible mechanism for choroidal thinning with increased myopia is atrophy and weakening of the choroidal large vessels due to axial stretching.[22,23] However, the relationship between thickness ratio and SER varied in different sublayers. Our finding of increased thickness ratio of SVCL and MVCL with SER indicates less thinning in these sublayers than in LVCL, perhaps reflecting relatively high shear stress on axial stretching in LVCL.[6,24,25] Moreover, the thick choroid primarily originated from LVCL thickening in children, suggesting that LVCL is associated with ocular growth or myopia development from another aspect.[26]

Measures of CV and VV enable choroidal vessel changes to be assessed from a three-dimensional perspective. Our findings suggest that the extent to which VV decreases with SER may vary across subfields. Previous research shows uneven regional characteristics of choroidal blood flow and vessel branching patterns.[16,27] Based on en face OCT, Savastano et al. summarized the proportions of five different vascular distribution patterns in LVCL. Among them, temporal herringbone pattern (49.2%), like those shown in Figures 5B and 5E, show that large vessels are more apparent in superior and inferior subfields.[16] Future research on the morphology of choroidal vascular distribution may help to understand the relationship among distribution patterns and refractive errors, age, ocular inflammatory, and vascular diseases.

Currently, almost all methods for quantifying choroidal vessels are based on binarization or shadow compensation. Differences in segmentation technology and binarization thresholds significantly influenced the estimation of choroidal lumen. Therefore, there are huge differences in CVI values between different studies.[21,28–30] Similar to our results, previous studies found that CVI values showed no correlation with SER and AL.[29,30] However, our results have also shown the VV decreases with SER and AL (Supplementary Table S12). The possible explanation is that both choroidal stromal and vascular area decreases proportionately in nonpathological myopia children.

As far as we know, this is the first research to realize automatic segmentation of choroidal sublayers and vessels in EDI-OCT images at the same time. Traditional gradient segmentation techniques for retinal sublayers are inappropriate because of the potential similarities between choroidal sublayers. In addition, tracking changes of pixel brightness costs much time when manually labeling choroidal sublayers boundaries and vessels. Our method can learn each pixel in labeled images, so as to improve the accuracy and repeatability.[31] Furthermore, previous study reported that artifacts of choriocapillaris and imaging depth may influence the estimation of CVD in en face SS-OCT and SS-OCTA.[31,32] However, based on vessels segmentation in B-scan images, our method could avoid their insufficiency of visualizing choroidal vessels, especially large vessels.

The limitations of our study are that it is retrospective and its sample size is small, with a narrow age range. Some factors that may affect choroidal morphology were not controlled, such as diurnal variation, water consumption, and caffeine.[17,28,33] Due to limited scanning mode, we studied the choroidal vascular structure only within 6 × 6 mm of the fovea. In addition, the choriocapillaris and choroidal small vessels in SVCL could not be analyzed due to the limitations of EDI-OCT. Further evaluation of both the choriocapillaris density and vascular area can be achieved by angio-OCT. Moreover, this study focused on healthy Asian children, so the results of this study cannot be directly applied to choroidal sublayer vascular structures of different ethnic groups or patients with ocular diseases.

In conclusion, our research shows the potential of deep learning and its advantages over standard image analysis methods. This automatic segmentation model helps to further study choroidal quantitative parameters between emmetropia and myopia. In future research, we plan to test our model in patients with retinal or choroidal diseases, modifying the model appropriately for more complex structural changes, to gradually expand application scope in eye diseases.

Disclosure: **J. Li**, None; **L. Zhu**, None; **R. Zhu**, None; **Y. Lu**, None; **X. Rong**, None; **Y. Zhang**, None; **X. Gu**, None; **Y. Wang**, None; **Z. Zhang**, None; **Q. Ren**, None; **B. Rong**, None; **L. Yang**, None

References

1. Rudnicka AR, Kapetanakis VV, Wathern AK, et al. Global variations and time trends in the prevalence of childhood myopia, a systematic review and quantitative meta-analysis: implications for aetiology and early prevention. *Br J Ophthalmol*. 2016;100:882–890.
2. Xu L, Wang Y, Li Y, et al. Causes of blindness and visual impairment in urban and rural areas in Beijing: the Beijing Eye Study. *Ophthalmology*. 2006;113:1134.e1–1134.11.
3. Chakraborty R, Read SA, Collins MJ. Monocular myopic defocus and daily changes in axial length and choroidal thickness of human eyes. *Exp Eye Res*. 2012;103:47–54.
4. Nickla DL, Wallman J. The multifunctional choroid. *Prog Retin Eye Res*. 2010;29:144–168.
5. Devarajan K, Sim R, Chua J, et al. Optical coherence tomography angiography for the assessment of choroidal vasculature in high myopia. *Br J Ophthalmol*. 2020;104:917–923.
6. Rayan A., Alshareef, et al. Choroidal vascular analysis in myopic eyes: evidence of foveal medium vessel layer thinning. *Int J Retina and Vitreous*. 2017;3:28.
7. Spaide RF, Koizumi H, Pozzoni MC. Enhanced depth imaging spectral-domain optical coherence tomography. *Am J Ophthalmol*. 2008;146:496–500.
8. Branchini LA, Adhi M, Regatieri CV, et al. Analysis of choroidal morphologic features and vasculature in healthy eyes using spectral-domain optical coherence tomography. *Ophthalmology*. 2013;120:1901–1908.
9. Adhi M, Brewer E, Waheed NK, Duker JS. Analysis of morphological features and vascular layers of choroid in diabetic retinopathy using spectral-domain optical coherence tomography. *JAMA Ophthalmol*. 2013;131:1267–1274.
10. Huang W, Zhang X. Morphology and Vascular Layers of the Choroid in Stargardt Disease Analyzed Using Spectral-Domain Optical Coherence Tomography. *Am J Ophthalmol*. 2015;160:1311.
11. Uppugunduri SR, Rasheed MA, Richhariya A, Jana S, Chhablani J, Vupparaboina KK. Automated quantification of Haller's layer in choroid using swept-source optical coherence tomography. *PLoS One*. 2018;13:e0193324.

12. Sonoda S, Terasaki H, Kakiuchi N, et al. Kago-Eye2 software for semi-automated segmentation of subfoveal choroid of optical coherence tomographic images. *Jpn J Ophthalmol*. 2019;63:82–89.

13. Mahajan NR, Donapati RC, Channappayya SS, Vanjari S, Richhariya A, Chhablani J. An automated algorithm for blood vessel count and area measurement in 2-D choroidal scan images. *Annu Int Conf IEEE Eng Med Biol Soc*. 2013;2013:3355–3358.

14. Sim DA, Keane PA, Mehta H, et al. Repeatability and Reproducibility of Choroidal Vessel Layer Measurements in Diabetic Retinopathy Using Enhanced Depth Optical Coherence Tomography. *Invest Ophthalmol Vis Sci*. 2013;54:2893–2901.

15. Otsu N. A Threshold Selection Method from Gray-Level Histograms. *IEEE Transactions on Systems Man & Cybernetics*. 2007;9:62–66.

16. Savastano MC, Rispoli M, Savastano A, Lumbroso B. En Face Optical Coherence Tomography for Visualization of the Choroid. *Ophthalmic Surg Lasers Imaging Retina*. 2015;46:561–565.

17. Gabriel M, Esmaeelpour M, Shams-Mafi F, et al. Mapping diurnal changes in choroidal, Haller's and Sattler's layer thickness using 3-dimensional 1060-nm optical coherence tomography. *Graefes Arch Clin Exp Ophthalmol*. 2017;255:1957–1963.

18. Okabe S, Matsuo N, Okamoto S, Kataoka H. Electron microscopic studies on retinochoroidal atrophy in the human eye. *Acta Medica Okayama*. 1982;36:11.

19. Quaranta M, Arnold J, Coscas G, et al. Indocyanine green angiographic features of pathologic myopia. *Am J Ophthalmol*. 1996;122:663–671.

20. Singh SR, Vupparaboina KK, Goud A, Dansingani KK, Chhablani J. Choroidal imaging biomarkers. *Surv Ophthalmol*. 2019;64:312–333.

21. Agrawal R, Ding J, Sen P, et al. Exploring choroidal angioarchitecture in health and disease using choroidal vascularity index. *Prog Retin Eye Res*. 2020;77:100829.

22. Cheng HM, Singh OS, Kwong KK, Xiong J, Woods BT, Brady TJ. Shape of the myopic eye as seen with high-resolution magnetic resonance imaging. *Optom Vis Sci*. 1992;69:698–701.

23. Moriyama M, Ohno-Matsui K, Futagami S, et al. Morphology and long-term changes of choroidal vascular structure in highly myopic eyes with and without posterior staphyloma. *Ophthalmology*. 2007;114:1755–1762.

24. Huo Y, Linares CO, Kassab GS. Capillary perfusion and wall shear stress are restored in the coronary circulation of hypertrophic right ventricle. *Circ Res*. 2007;100:273–283.

25. Puri R, Leong DP, Nicholls SJ, et al. Coronary artery wall shear stress is associated with endothelial dysfunction and expansive arterial remodelling in patients with coronary artery disease. *EuroIntervention*. 2015;10:1440–1448.

26. Park KA, Oh SY. An optical coherence tomography-based analysis of choroidal morphologic features and choroidal vascular diameter in children and adults. *Am J Ophthalmol*. 2014;158:716–723 e712.

27. Yoneya S, Tso MO. Angioarchitecture of the human choroid. *Arch Ophthalmol*. 1987;105:681–687.

28. Betzler BK, Ding J, Wei X, et al. Choroidal vascularity index: a step towards software as a medical device [published online ahead of print January 29, 2021]. *Br J Ophthalmol*, https://doi.org/10.1136/bjophthalmol-2021-318782.

29. Singh SR, Invernizzi A, Rasheed MA, et al. Widefield Choroidal Vascularity in Healthy Eyes. *Am J Ophthalmol*. 2018;193:100–105.

30. Abhilash Goud, Sumit, et al. New Insights on Choroidal Vascularity: A Comprehensive Topographic Approach. *Invest Ophthalmol Vis Sci*. 2019;60:3563–3569.

31. Sekiryu T, Sugano Y, Ojima A, et al. Hybrid Three-Dimensional Visualization of Choroidal Vasculature Imaged by Swept-Source Optical Coherence Tomography. *Transl Vis Sci Technol*. 2019;8:31.

32. Wang JC, Lains I, Silverman RF, et al. Visualization of Choriocapillaris and Choroidal Vasculature in Healthy Eyes With En Face Swept-Source Optical Coherence Tomography Versus Angiography. *Transl Vis Sci Technol*. 2018;7:25.

33. Mansouri K, Medeiros FA, Marchase N, Tatham AJ, Auerbach D, Weinreb RN. Assessment of choroidal thickness and volume during the water drinking test by swept-source optical coherence tomography. *Ophthalmology*. 2013;120:2508–2516.